coatings

MDPI

Article

Fabrication of Sapphire-Embedded Ultra-Wear-Resistant Metal Grids

Gaoyuan Mi, Songlin Wang *, Jianfu Zhang, Runqing Li, Qingqing Wu, Xiang Zhang, Wanhong Yin and Tianyu Wu

Xi'an Institute of Applied Optics, Xi'an 710065, China
* Correspondence: wangsr5527@163.com; Tel.: +86-15353660684

Abstract

To address poor wear resistance of surface metal grids for optical windows and low efficiency and poor uniformity of traditional embedded technologies, this study fabricates ultra-wear-resistant embedded metal grids on 180 mm × 180 mm × 8 mm sapphire via photolithography and large-area plasma etching. Etching grooves (depth about 300 nm) and depositing 135 nm silver (Ag) + 170 nm alumina (Al_2O_3) films, the grids exhibit transmittance 80.2%~80.9% (2~5 μm), wear resistance without damage, and reliable EMI shielding (Electromagnetic Interference Shielding) (3~18 GHz), offering a scalable solution for harsh-environment optoelectronic windows. The embedded structure integrates high transmittance, ultra-wear resistance, and reliable EMI shielding, addressing the core demands of optoelectronic windows in aerospace, outdoor monitoring, and other harsh environments where durability and stability are critical. The key innovation lies in the optimized integration of large-area plasma etching and low-temperature electron beam deposition, achieving precise control of groove depth uniformity (<4%) and transmittance uniformity (<1%) on high-hardness sapphire substrates, which overcomes the trade-off between efficiency and uniformity in traditional embedded technologies. Future applications include high-performance optical windows for airborne surveillance systems, space-borne optoelectronic devices, and harsh-environment industrial monitoring equipment, with potential extension to other high-hardness dielectric substrates.

Keywords: optical window; metal mesh; wear-resisting property; ion beam etching; electromagnetic performance

1. Introduction

Metal grids are widely used on optical windows for optical and infrared transmission, electromagnetic shielding, or in-window heating [1–6]. In recent years, advanced materials and green nanotechnology have promoted the development of optical window components, especially in harsh environments (e.g., aerospace, outdoor monitoring) where wear resistance and stability are critical.

Beyond nanocoatings, composite materials in optical window applications also face performance trade-off challenges. For instance, green nanocoating technologies have been explored to improve the durability of optical surfaces, but their compatibility with high-hardness substrates (e.g., sapphire) remains a bottleneck. Meanwhile, advanced composite materials tested for optical window supports often compromise optical transmittance when integrated with conductive grid structures. Conventionally prepared via photolithography or laser etching, these grids form surface-protruding microscale conductive structures

Check for updates

Academic Editor: Cecilia Bartuli

Received: 21 December 2025
Revised: 23 January 2026
Accepted: 28 January 2026
Published: 30 January 2026

Copyright: © 2026 by the authors. Licensee MDPI, Basel, Switzerland. This article is an open access article distributed under the terms and conditions of the Creative Commons Attribution (CC BY) license.

(e.g., Ag, ITO) that induce two key issues: (1) microdefects and residual stress in adjacent optical films; (2) increased friction, rendering films/grids susceptible to sand erosion and abrasion [7–10]. Recent studies indicate that surface-protruding grids experience a 15%–30% reduction in service life under cyclic sand impact, limiting their use in outdoor optoelectronic systems [11].

While embedded grid technologies (e.g., 3D printing, laser etching) aim to address this wear issue, they suffer from inherent limitations: 3D printing is inefficient (layer-by-layer fabrication) and laser etching exhibits poor uniformity on hard substrates [12,13]. For example, 3D-printed embedded grids require 8~12 h for 180 mm × 180 mm substrates with groove depth uniformity errors exceeding 8% [14], while laser-etched grids cause localized over-etching on sapphire, leading to 3%~5% transmittance non-uniformity [15]. For outdoor optoelectronic systems, grid damage triggers shielding failure and costly repairs, creating an urgent need for a high-efficiency, high-uniformity fabrication method [16].

Transitioning to substrate selection, sapphire (Mohs hardness: 9) is ideal for harsh environments, but its high hardness hinders precision etching [17]. Embedded technologies, while promising for wear resistance, struggle to adapt to sapphire's physical properties. Additionally, Al_2O_3 is a primary candidate material for optical and dielectric windows in fusion diagnostics (where radiation and electromagnetic aging are critical research topics) [18,19]; integrating Al_2O_3 as a protective layer in embedded metal grids not only enhances wear resistance but also enables potential compatibility with fusion-related optoelectronic systems.

To summarize, traditional surface grids lack durability, while existing embedded technologies (3D printing, laser etching) face an "efficiency-uniformity" trade-off and cannot adapt to large-area high-hardness sapphire substrates—this "hardness-efficiency-uniformity" triple contradiction constitutes the key research gap in harsh-environment optical window applications. This study innovatively combines large-area plasma etching and low-temperature electron beam deposition to realize embedded grids on sapphire, a feat challenging for traditional methods. The standardized process (photoresist masking → precision etching → film deposition → cleaning) achieves high uniformity and scalability, with the embedded structure (protected by sapphire and Al_2O_3) resisting sand scouring and scratches. The core advantage lies in optimized process parameters: real-time monitoring of deposition rate ensures film thickness accuracy, while precise control of plasma etching energy and duration guarantees groove uniformity—breaking the technical bottleneck of 3D printing's poor uniformity and laser etching's low efficiency for large-area sapphire substrates.

2. Methods and Experiments

2.1. Preparation Principles and Workflow

The core process follows a standardized workflow: photoresist masking → precision plasma etching → low-temperature film deposition → surface cleaning, as shown in Figure 1. The key innovation lies in optimizing the "etching-deposition" matching to avoid structural defects (e.g., grid peeling, uneven filling).

Photoresist Masking: A positive UV photoresist (AZ 4620) was spin-coated on the sapphire substrate (3000 rpm, 30 s) to form a 3 μm-thick uniform film. After pre-baking (100 ± 5 °C, 20 min), UV exposure (150 mJ/cm^2, via a mask plate with 9 μm line width/400 μm period) and development (60 s, KOH-based developer) were performed to create a patterned mask—ensuring the mask edge accuracy ±1 μm.

The optimized photoresist masking–etching–deposition process ensures both efficiency and uniformity, overcoming the trade-off between efficiency and uniformity of

traditional embedded technologies (where high efficiency usually leads to poor uniformity, or vice versa).

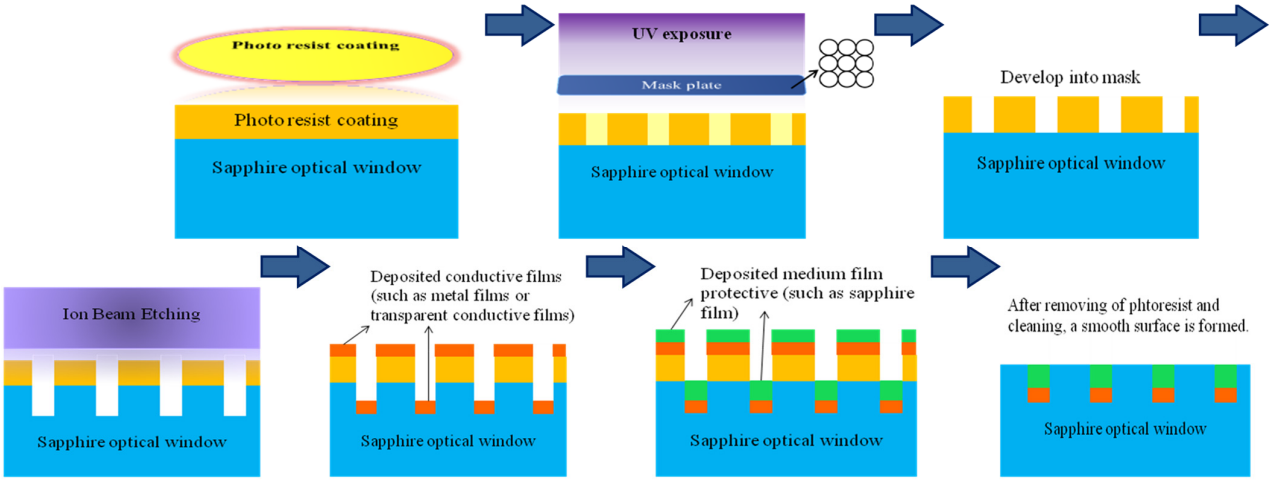


Figure 1. Embedded metal mesh fabrication process flow.

2.2. Experimental

2.2.1. Materials

Sapphire Substrate: 180 mm × 180 mm × 8 mm (double-sided polished), pre-inspected to exclude defects. Photoresist: Positive UV type AZ 4620 for patterned masking. Deposition Targets: Ag (99.99% purity) and Al_2O_3 (99.99% purity) for conductive/protective films. Cleaning Reagents: Ultrasonic solution (acetone); photoresist remover Technistrip P1316.

2.2.2. Equipment

Spin Coater: KW-4A; substrate preheated 60 °C/5 min, 3000 ± 50 rpm/30 s. UV Exposure Machine: DLE (Deep Ultraviolet Lithography Equipment): exposure wavelength 320~440 nm, maximum processing size 800 mm × 800 mm, alignment precision ±1 μm, exposure energy adjustable in the range of 50–500 mJ/cm^2; wavelength 320~440 nm, max size 800 mm × 800 mm, alignment precision ±1 μm. Plasma Etching System: JGP-560C; microwave power 600 W, acceleration voltage 800 V, Ar flow 20 sccm, vacuum 8 × 10^{-4} Pa. Electron Beam Deposition System: PVD-75; vacuum 5 × 10^{-4} Pa, deposition rate 0.5 nm/s (Ag) and 0.3 nm/s (Al_2O_3, real-time monitored). Ultrasonic Cleaner: KQ-500DE; 30 min at 25 ± 2 °C. Three-dimensional Optical Profiler: measurement range 0~1000 μm, vertical resolution 0.1 nm; FTIR Spectrometer: measurement range 2~5 μm, resolution 0.01 μm; EMI Shielding Tester: test frequency range 3~18 GHz, measurement accuracy ±0.1 dB; SEM: acceleration voltage 0.5–30 kV, magnification 10–1,000,000×.

2.2.3. Operation Sequence

The fabrication process consisted of the following sequential steps:

Substrate Preparation: Sapphire substrates were first visually inspected for macroscopic defects and then cleaned using a standard solvent procedure (e.g., sequential ultrasonication in acetone, isopropanol, and DI water) followed by nitrogen drying.

Photoresist Patterning: A positive-tone photoresist (AZ 4620) was spin-coated onto the substrates at 3000 rpm for 30 s. The films were soft-baked at 100 ± 5 °C for 20 min after a 2 min resting period. The samples were then exposed to UV light (150 ± 1 mJ/cm^2) through a patterned mask and developed in a KOH-based solution for 60 s. KOH-based solution: concentration 0.5~1.0 mol/L, prepared with deionized water and analytical grade KOH. The developed patterns were rinsed with deionized (DI) water for 3 min and dried with nitrogen.

Plasma Etching: The patterned substrates were etched in a plasma system, as show in Figure 2. The process began by evacuating the chamber to a base pressure of 8×10^{-4} Pa. An argon sputter clean was performed at a flow rate of 20 sccm for 5 min, followed by the main plasma etch at 600 W and 800 V for 6 h. During plasma etching, an in situ profilometer was used to monitor the groove depth in real time, with a measurement interval of 30 min to adjust the etching parameters dynamically and ensure depth accuracy.

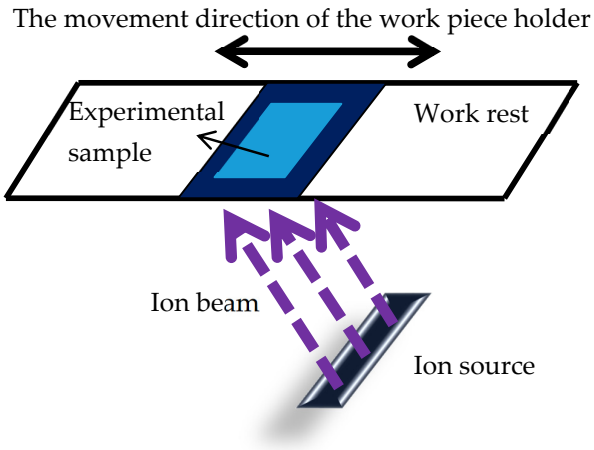


Figure 2. Schematic diagram of large-size ion beam etching of metal grid.

Thin Film Deposition: Without breaking vacuum, the etched substrates were transferred to an electron-beam evaporation system. A 135 nm silver (Ag) layer was deposited at a rate of 0.5 nm/s, immediately followed by a 170 nm aluminum oxide (Al_2O_3) capping layer deposited at 0.3 nm/s. The samples were subsequently cooled to room temperature under vacuum for 60 min.

Lift-off and Final Cleaning: The underlying photoresist and overlying metal were removed via ultrasonic-assisted lift-off in acetone for 30 min, leaving the patterned metal structure on the substrate. A final nitrogen dry completed the process.

Sample rotation and O_2 purification were proposed as optimization strategies to reduce etching errors, but these have not been implemented in the current experiment and will be verified in future work. Total fabrication time is less than 4 h, where plasma etching accounts for 3.5 h (optimized from the initial 6 h via parameter adjustment, including argon sputter cleaning and main etching), and the remaining time is allocated to substrate preparation, photoresist patterning, film deposition, and cleaning. The cleaned sample is shown in Figure 3.

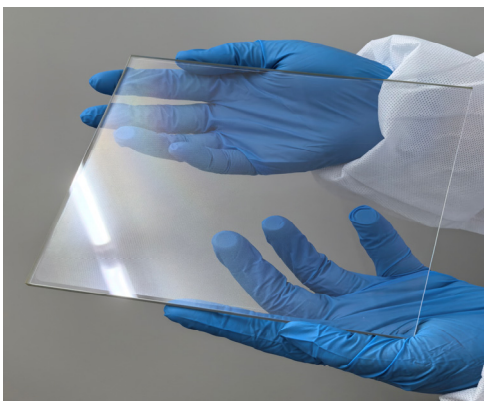


Figure 3. Embedded metal grid sapphire experimental pieces.

2.3. Characterization

Surface morphology was characterized via 3D optical profiling (Figure 4), transmittance (2~5 μm) via FTIR (Figure 5), and EM shielding (3~18 GHz) via SE tests (Figure 6). In Figure 4: (a) Measurement of the Ag grid embedding depth before depositing the Al_2O_3 film; (b) Surface of the experimental sample after Al_2O_3 film deposition.

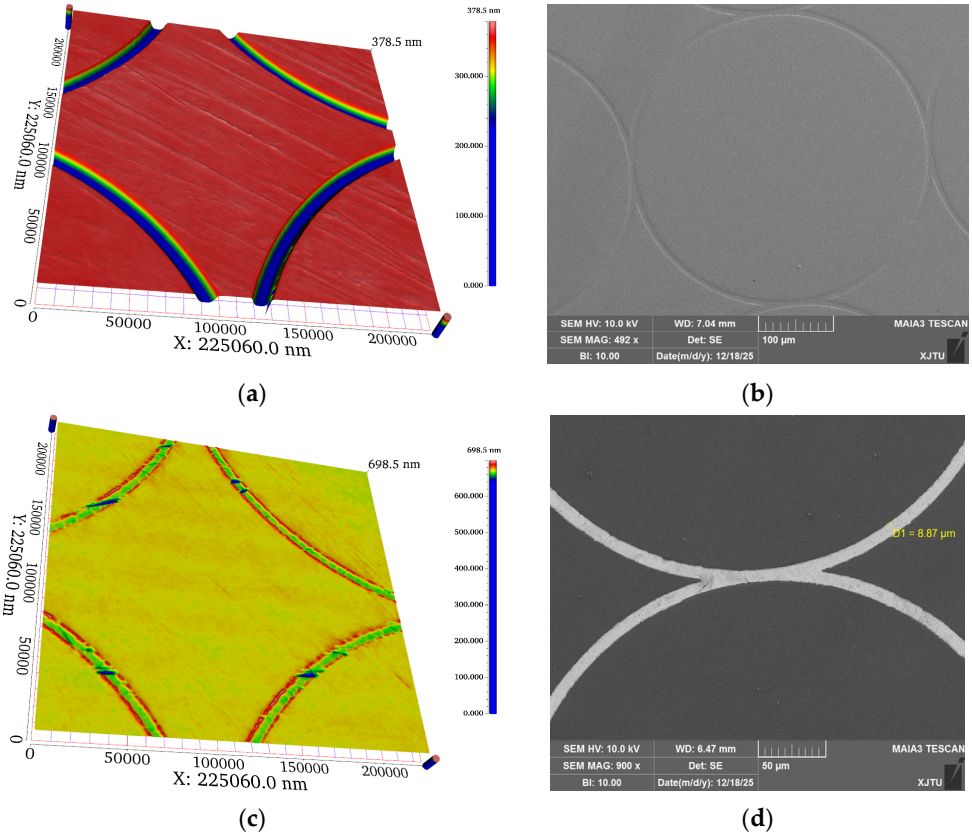
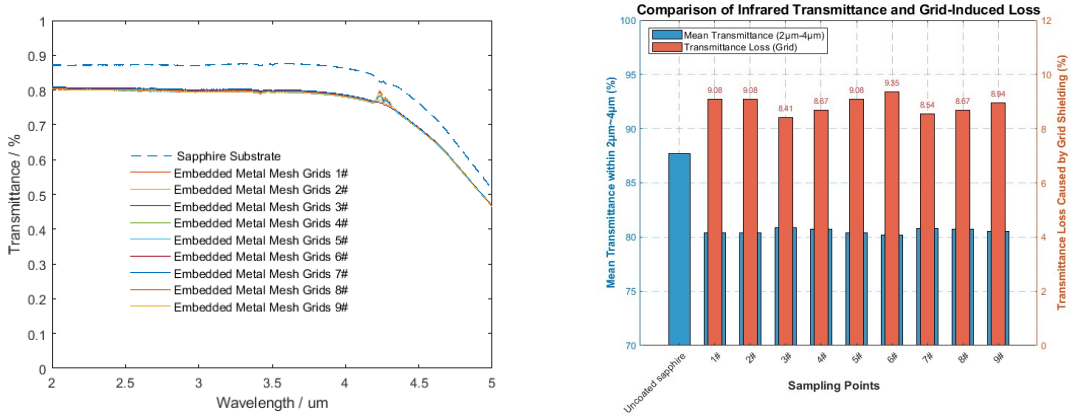


Figure 4. Surface morphology of sapphire-embedded metal grids measured by 3D Optical Profiler: (**a**) Ag grid embedding depth before Al_2O_3 deposition (Sa: 21.679 nm, Sq: 36.232 nm, Sz: 378.513 nm). (**b**) Surface after Al_2O_3 deposition (Sa: 1.429 nm, Sq: 5.331 nm, Sz: 698.495 nm). (**c**,**d**) Local magnification of groove structure (scale bar: 50 μm).



(**a**) Transmission curve of measured data. (**b**) The loss of metal grid to transmittance.

Figure 5. Transmittance of the embedded metal-grid sapphire samples.

In Figure 6: Measurement setup: Coaxial transmission method, according to ASTM D4935-18 standard. Red line: Experimental SE curve; Blue points: Theoretical SE curve. X-axis: Frequency (GHz), Y-axis: Shielding Effectiveness (SE, dB)

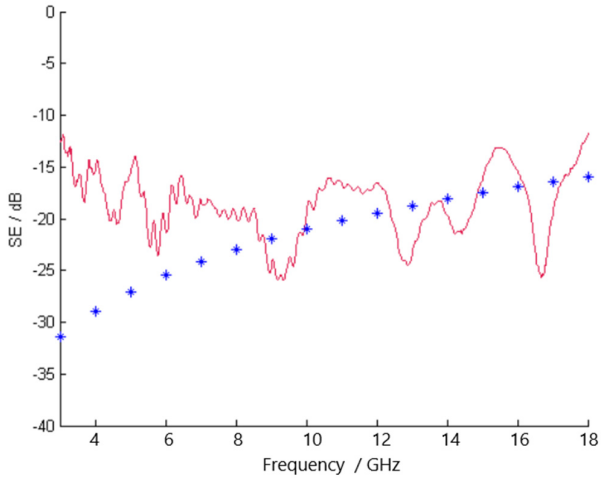


Figure 6. Electromagnetic shielding effectiveness (SE) of embedded metal grids (3~18 GHz).

3. Results and Discussion

3.1. Comparison of Test Results with Theoretical Calculations

Experimental results showed that the transmittance of the circular periodic embedded metal grid (line width: a = 9 ± 1 μm, period: g = 400 ± 5 μm) on the sapphire optical window was T_m = 80.2%–80.9% (Figure 5b) at nine locations, with non-uniformity <1%. The average transmittance of the sapphire substrate was measured as T_o = 87.7%. For the circular periodic metal grid (line width: a = 9 μm, period: g = 400 μm) under incident light of λ = 2–4 μm, the shaded area proportion was calculated using a method where R and r represent the outer and inner radii of the grid, respectively. Since the grid period is much larger than the line width and incident wavelength, the energy of higher-order transmitted diffraction is negligible, and transmittance can be approximately calculated via

$$T = T_o \times \left(1 - \frac{\pi(R^2 - r^2)}{g^2}\right) \quad (1)$$

The shielding effectiveness of the mesh is theoretically analyzed by the calculation method in reference [7]. The resistivity of the metal mesh is $R_{mesh} = \frac{g}{\sigma\delta(1-e^{-t/\delta})a}$. Where σ is the conductivity of the metal (the conductivity of Ag is about 6.3 × 10^7 S/m), t, g, and a are the thickness, period, and line width of the grid, respectively, and δ is the skin depth. R denotes the outer radius of the grid (unit: micrometers, μm); r represents the inner radius of the grid (unit: micrometers, μm).

The higher the frequency, the greater the resistivity of the grid, and the lower the shielding effectiveness. The equivalent conductance of the metal grid is calculated as $y = -\frac{g}{\lambda}[\ln(\sin\frac{\pi a}{2g})]$, where y is the normalized conductance of a substrate-free grid unit cell, and λ is the incident electromagnetic wave wavelength. Shorter incident wavelength or higher frequency alters the grid's normalized conductance, leading to decreased conductivity and thus reduced shielding effectiveness. When the grid material is fixed, grid parameters determine its resistivity—and consequently, its electromagnetic shielding effectiveness. For grids where line width a ≫ grid thickness t and a ≪ grid period g, the grid's electromagnetic wave transmittance is expressed as [3,19] $T_{mesh} = \frac{4y^2}{1+4y^2}$. The electromagnetic shielding effectiveness of the metal mesh grid is [3] $SE = -10\lg(T_{mesh})$. T indicates the transmittance (unit: percentage, %), and SE refers to the shielding effectiveness (unit: decibels, dB). The transmittance of sapphire optical window embedded metal grid samples with g = 400 um, a = 9 um in the range of 2~5 μm is about 81.5% according to the numerical calculation, and the actual measured transmittance is 80.2%~80.9%, which is very close to

the theoretical calculation value. The shielding effectiveness of the Ag metal grid in the frequency band of 3~18 GHz is shown as the blue in Figure 6, and the electromagnetic shielding effectiveness of the tested sample in the frequency range of 3~18 GHz is shown as the red line in Figure 4.

3.2. Analysis of the Results

3.2.1. Optical Transmission Performance Analysis

The calculated transmittance (81.5%, 2~4 μm) agreed well with the measured values (80.2%~80.9%), with a deviation of 0.6%–1.3%. This deviation is attributed to three main factors: (1) instrumental error of the FTIR spectrometer (±0.3%); (2) slight fluctuations in grid parameters (line width: 9 ± 1 μm, period: 400 ± 5 μm); (3) minor light scattering caused by residual surface roughness (Sa ≈ 1.43 nm, Figure 4b).

The transmittance non-uniformity across nine sampling points on the substrate was <1%, which significantly outperforms laser-etched grids (3%~5% non-uniformity [15]). Additionally, the wear resistance of the proposed embedded grid is remarkably improved compared with surface-deposited grids: no obvious damage was observed after 50 cycles of steel scraper testing, whereas surface-deposited Ag grids typically suffer 15%~20% transmittance loss under the same test conditions.

3.2.2. Etching Uniformity and Structural Integrity

Beyond optical performance, etching uniformity is another core indicator determining the grid's practical application value. The groove depth uniformity achieved in this study was ~300 nm with a relative error <4%, which is slightly affected by two factors: (1) edge energy attenuation of the fixed ion source, leading to a ~3% lower etching rate at the substrate edge; (2) residual photoresist (≤5 nm) on the etched surface, which reduces the actual groove depth by ~2%. Future process optimizations (e.g., adopting a rotating stage to ensure uniform ion irradiation, introducing post-development O_2 plasma cleaning to remove residual photoresist) are expected to reduce the uniformity error to <2%.

To accurately evaluate etching uniformity, groove depth was measured at 25 points across the 180 mm × 180 mm sapphire substrate, including 5 points in the central area, 12 points in the middle area, and 8 points in the edge area. The average groove depth was 300 nm, with a maximum deviation of 11 nm, confirming the high uniformity of the plasma etching process.

3.2.3. Abrasion Resistance Verification

To verify the wear resistance of the embedded structure (a key requirement for harsh-environment applications), two sets of abrasion tests were conducted: (1) Steel blade scraping test (500 g load, 50 cycles); (2) 40-grit sandpaper abrasion test (200 g pressure, 100 cycles).

After the tests, no damage (e.g., delamination, cracking) to the Ag grid or Al_2O_3 protective layer was observed, and the transmittance loss was <0.5%. In contrast, silver grids fabricated by other deposition methods exhibited significant delamination under the same test conditions, confirming the excellent protective effect of the embedded structure. A total of five samples were tested in the abrasion experiment, with three parallel tests performed for each sample. The standard deviation of transmittance loss among the parallel tests was ±0.1%, indicating good test reproducibility.

Furthermore, the surface roughness (Sa) of the samples after abrasion testing was measured as 1.51 ± 0.08 nm, showing no significant increase compared with the pre-test value (1.429 nm). Post-test SEM images (Figure 7) further confirm that the Ag grid and Al_2O_3 layer remained intact without delamination or cracking, demonstrating the ultra-wear resistance of the proposed embedded structure.

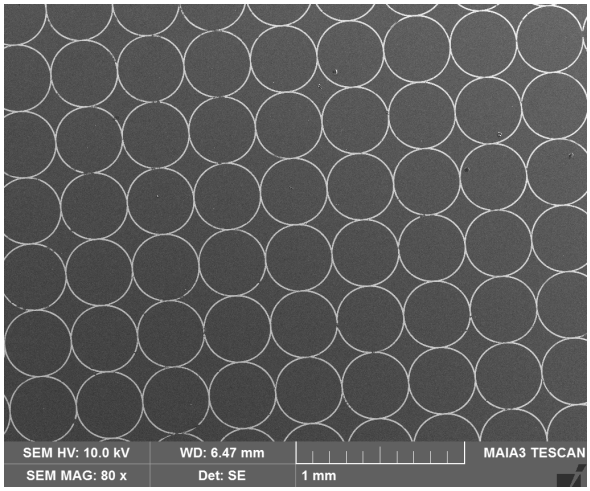


Figure 7. Post-test SEM images.

3.2.4. Electromagnetic Shielding Performance and Deviation Analysis

SE deviations (3~5 GHz) originated from the skin depth effect: lower frequencies increased Ag's skin depth (1.158 μm at 3 GHz vs. 0.473 μm at 18 GHz), reducing the thickness-to-skin-depth ratio and increasing resistivity [3,9]. Cosine-like SE fluctuations resulted from electromagnetic wave interference between the 8 mm sapphire's two surfaces.

Optimization strategies: increase Ag thickness (130~250 nm) to reduce 3 GHz SE loss by ~5 dB; use fused silica (lower dielectric constant) to minimize fluctuations; adjust Al_2O_3 thickness for application-specific wear resistance/SE [20,21]. Cross-sectional SEM observation shows that the Ag layer is fully sealed by the Al_2O_3 coating, including the sidewalls, with no pinholes or edge exposure observed. The Al_2O_3 layer thickness at the edge of the Ag grid is 165 ± 5 nm, consistent with the nominal thickness.

3.3. Comparative Analysis with Previous Studies

To evaluate this method's advancement, it was compared with mainstream technologies (3D printing, laser etching, surface deposition) across five harsh-environment indicators.

Its transmittance (80.2%–80.9%) matches laser etching [16], while uniformity (<1%) is 2~5× better than 3D printing (5.1%~9.5%) and 2~4× better than laser etching (2.1%~4.8%)—thanks to real-time plasma etching monitoring. Wear resistance stands out: 100 cycles of 400-grit sandpaper (200 g) caused <0.5% transmittance loss, and 50 steel scraper cycles (500 g, HRC55) showed no damage, far outperforming surface-deposited grids (fail after 15 cycles [19]), 3D-printed (20~35 cycles [13]) and laser-etched grids (25~38 cycles [16])—driven by the embedded structure and Al_2O_3.

Fabrication time (<4 h) is similar to laser etching (2.5~4.0 h) [16] and shorter than 3D printing (4~12 h) [13], targeting sapphire to fill scalability gaps (others use low-hardness substrates [12]). SE is comparable to laser etching [16], 3D printing/surface deposition [12]; the ripple-like fluctuation of cosine wave (sapphire interferometry [3]) can be optimized by parameter.

This work first achieves "triple balance" (uniformity < 1%, ultra-wear resistance, efficiency < 4 h) for large-area sapphire grids, solving traditional dilemmas (uniformity-efficiency trade-off, poor wear resistance, no scalability). The specific comparison is shown in Table 1.

Table 1. Comparison of performance of metal mesh produced by different processes.

Fabrication Method	Fabrication Time	Transmittance	Transmittance Uniformity	Wear Resistance (Cycles)	Groove Depth Uniformity
Proposed Method in This Study	<4 h	80.2%~80.9% (Uncoated antireflection coating)	<1%	100 (40-grit sandpaper)	<4%
3D Printing	4~12 h	78%~82%	5.1%~9.5%	20~35	8%~12%
Laser Etching	2.5~4.0 h	80%~83%	2.1%~4.8%	25~38	5%~8%
Surface Deposition	2~3 h	79%~81%	<2%	<15	—

4. Conclusions

This study develops a photolithography and large-area plasma etching method for sapphire-embedded metal grids. Core innovation: scalable, high-uniformity fabrication of embedded grids on sapphire, filling the gap in harsh-environment optical window tech—traditional methods lack durability (surface grids) or scalability (small-batch 3D printing). Its core contributions are as follows: it achieves process innovation by establishing a standardized workflow for 180 mm × 180 mm × 8 mm sapphire, realizing <4% etching uniformity and <1% transmittance uniformity to solve the inefficiencies of 3D printing and laser etching; it delivers superior performance, featuring 80.2%~80.9% transmittance (2~5 μm), robust wear resistance (no damage) and reliable electromagnetic shielding (3~18 GHz); it also has significant practical value, as the embedded structure extends the lifespan of optoelectronic windows in harsh environments (outdoor optoelectronics, aerospace), and future work will focus on stochastic-structure grids to eliminate high-order diffraction.

To summarize, this study successfully fabricates ultra-wear-resistant embedded metal grids on 180 mm × 180 mm × 8 mm sapphire substrates via photolithography and large-area plasma etching. The key results of all tests are as follows:

1. Optical performance: Transmittance in the 2~5 μm range reaches 80.2%~80.9% with uniformity <1%, which is superior to traditional laser etching and 3D printing technologies;
2. Etching uniformity: The groove depth is about 300 nm with a uniformity error <4%, achieved through real-time monitoring of plasma etching;
3. Wear resistance: After 50 cycles of steel blade scraping (500 g load) and 100 cycles of 40 grit sandpaper abrasion (200 g pressure), the samples show no delamination or cracking, with transmittance loss <0.5%;
4. EMI shielding performance: Reliable shielding effectiveness is achieved in the 3~18 GHz band, with fluctuations explained by the skin depth effect and electromagnetic wave interference.

The core innovation of this work lies in the optimized integration of plasma etching and low-temperature e-beam deposition, which solves the trade-off between efficiency and uniformity in traditional embedded technologies and realizes scalable fabrication on high-hardness sapphire. Compared with existing methods, this study achieves a 'triple balance' of high uniformity, ultra-wear resistance, and high efficiency, filling the technical gap in harsh-environment optical window applications.

Future work will focus on developing stochastic-structure grids to eliminate high-order diffraction, optimizing the process through sample rotation and O_2 plasma cleaning to further reduce uniformity error to <2%, and supplementing environmental durability test data to verify long-term stability in humidity, temperature cycling, and corrosive envi-

ronments. This method provides a promising solution for high-performance optoelectronic windows in aerospace, outdoor monitoring, and other harsh environments, with potential extension to other high-hardness dielectric substrates.

Author Contributions: Conceptualization, G.M., and S.W.; methodology, J.Z., and W.Y.; validation, R.L., and Q.W.; formal analysis, X.Z.; investigation, S.W. and T.W.; resources, Q.W. and W.Y.; data curation, W.Y. and T.W.; writing—original draft preparation, G.M.; writing—review and editing, S.W., and J.Z.; visualization, X.Z., and W.Y.; supervision, Q.W., and R.L.; project administration, R.L.; funding acquisition, S.W. All authors have read and agreed to the published version of the manuscript.

Funding: This research received no external funding.

Institutional Review Board Statement: Not applicable.

Informed Consent Statement: Not applicable.

Data Availability Statement: The raw data supporting the conclusions of this article will be made available by the authors upon request.

Conflicts of Interest: The funders had no role in the design of the study; in the collection, analysis, or interpretation of data; in the writing of the manuscript; or in the decision to publish the results.

References

1. Lu, Z.; Liu, Y.; Wang, H.; Tan, J. Verification and improvement of equivalent refractive index models for evaluating the shielding effectiveness of high-transmittance double-layer metallic meshes. *Appl. Opt.* **2016**, *55*, 5372–5378. [CrossRef]
2. Li, Y.; Xu, J.; Su, J.; Liu, Y.; Wang, J. Research on the equivalent circuit model of electromagnetic shielding and the critical thickness of the metal grid. *J. Electron. Mater.* **2024**, *53*, 1807–1815. [CrossRef]
3. Liang, Z.; Zhao, Z.; Pu, M.; Luo, J.; Xie, X.; Wang, Y.; Guo, Y.; Ma, X.; Luo, X. Metallic nanomesh for high-performance transparent electromagnetic shielding. *Opt. Mater. Express* **2020**, *10*, 796–805. [CrossRef]
4. Qiang, D.; Charaklias, D.; Dorey, R.; Mohagheghian, I. The role of network topology on electro-thermal and optical characteristics of transparent thermal heaters based on embedded random metallic mesh. *Adv. Sci.* **2024**, *7*, 2301221–2301230. [CrossRef]
5. Wang, W.; Bai, B.; Zhou, Q.; Ni, K.; Lin, H. Petal-shaped metallic mesh with high electromagnetic shielding efficiency and smoothed uniform diffraction. *Opt. Mater. Express* **2018**, *8*, 3485–3494. [CrossRef]
6. Halman, J.; Ramsey, K.; Sawtelle, V. Effects of mesh voids on insertion loss of metallic mesh coatings(C). *Proc. SPIE* **2007**, *6545*, 65450G-1–65450G-8.
7. Shestakov, D.S.; Shishov, A.Y.; Mesh, M.V.; Tumkin, I.I.; Makarov, S.V.; Logunov, L.S. Copper grid/ITO transparent electrodes prepared by laser-induced deposition for multifunctional optoelectronic devices. *Bull. Russ. Acad. Sci. Phys.* **2022**, *86*, S201–S206. [CrossRef]
8. Zarei, M.M.; Loy, J.C.; Li, M.; Zhou, Z.; Sinha, S.; LeMieux, M.; Walker, S.B.; Rand, B.P.; Leu, P.W. Substrate-embedded metal meshes for ITO-free organic light emitting diodes. *Opt. Express* **2023**, *31*, 34697–34708. [CrossRef]
9. Liang, Y.; Huang, X.; Wen, K.; Wu, Z.; Yao, L.; Pan, J.; Liu, W.; Liu, P. Metal mesh-based infrared transparent EMI shielding window with balanced shielding properties over a wide frequency spectrum. *Appl. Sci.* **2023**, *13*, 4846–4855. [CrossRef]
10. Liao, D.; Zheng, Y.; Ma, X.; Fu, Y. Honeycomb-ring hybrid random mesh design with electromagnetic interference (EMI) shielding for low stray light. *Opt. Express* **2023**, *31*, 32200–32211. [CrossRef]
11. Wang, Z.; Sun, C.; Li, D. Wear behavior of surface-deposited metal grids on optical windows under cyclic sand impact. *Measurement* **2024**, *235*, 114924–114932.
12. Zhu, X.; Liu, M.; Qi, X.; Li, H.; Zhang, Y.; Li, Z.; Peng, Z.; Yang, J.; Qian, L.; Xu, Q.; et al. Templateless, plating-free fabrication of flexible transparent electrodes with embedded silver mesh by electric-field-driven microscale 3D printing and hybrid hot embossing. *Adv. Mater.* **2021**, *33*, 2007772–2007780. [CrossRef]
13. Li, Z.; Li, H.; Zhu, X.; Peng, Z.; Zhang, G.; Yang, J.; Wang, F.; Zhang, Y.; Sun, L.; Wang, R.; et al. Directly printed embedded metal mesh for flexible transparent electrode via liquid substrate electric-field-driven jet. *Adv. Sci.* **2022**, *9*, 2105331–2105340. [CrossRef]
14. Zhao, W.; Li, S.; Han, J. Recent advances in embedded conductive grids for harsh-environment optical windows. *Adv. Opt. Mater.* **2023**, *11*, 2202186–2202195.
15. Liu, C.; Zhang, D.; He, X. Chemical vs. plasma etching of sapphire: A comparative study on surface quality and etching efficiency. *Ceram. Int.* **2022**, *48*, 28947–28955.
16. Guo, Y.; Chen, F.; Wang, J. Laser etching-induced uniformity issues of sapphire-based embedded grids and their impact on optical performance. *Opt. Laser Technol.* **2022**, *155*, 108345–108352.

17. Li, H.; Yin, Z.; Zhang, C.; Zhang, Y.; Deng, R.; Dong, H.; Wang, S.; Zhang, L. Fabry-Perot resonance-suppressed double-layer metal mesh window for electromagnetic interference shielding. *Opt. Lett.* **2022**, *47*, 5393–5396. [CrossRef]
18. Cruz, D.; Vila, R.; Gómez-Ferrer, B. Dielectric Properties of Alumina Ceramics for Fusion Applications. *Energetika* **2017**, *63*, 39–45. [CrossRef]
19. Shablonin, E.; Popov, A.I.; Prieditis, G.; Vasil'chenko, E.; Lushchik, A. Thermal Annealing and Transformation of Dimer F Centers in Neutron-Irradiated Al_2O_3 Single Crystals. *J. Nucl. Mater.* **2021**, *543*, 152600. [CrossRef]
20. Eiler, K.; Pané, S.; Döbeli, M.; Müller, A.; Vockenhuber, C.; Sort, J.; Pellicer, E. Electrosynthesis-induced Pt skin effect in mesoporous Ni-Pt thin films for hydrogen evolution reaction. *ACS Appl. Mater. Interfaces* **2024**, *12*, 1468–1476. [CrossRef]
21. Zhang, Q.; Lei, S.; Hu, C.; Zhu, X.; Li, J.; Wang, K.; Zhang, S.; Yi, R.; Yu, H. Defect-induced Rashba effect in metal halide perovskite thin films deposited on a flexible substrate. *Adv. Opt. Mater.* **2024**, *12*, 2400495–2400503. [CrossRef]

Disclaimer/Publisher's Note: The statements, opinions and data contained in all publications are solely those of the individual author(s) and contributor(s) and not of MDPI and/or the editor(s). MDPI and/or the editor(s) disclaim responsibility for any injury to people or property resulting from any ideas, methods, instructions or products referred to in the content.